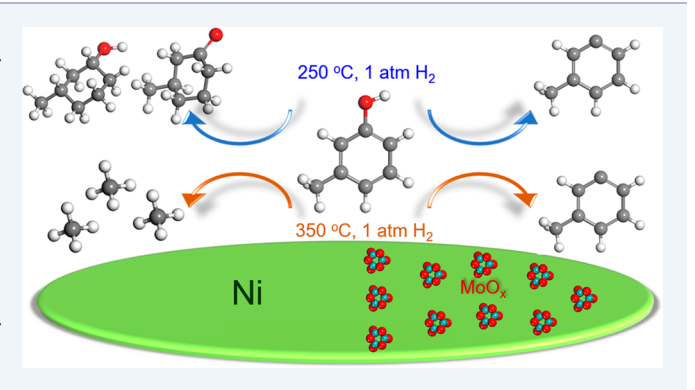


Enhancement of m-Cresol Hydrodeoxygenation Selectivity on Ni Catalysts by Surface Decoration of MoO_x Species

Feifei Yang, †,‡ Nicole J. Libretto, Mallikharjuna Rao Komarneni,‡ Wei Zhou,† Jeffrey T. Miller, * Xinli Zhu,*^{,†} and Daniel E. Resasco*^{,‡}

Supporting Information

ABSTRACT: Catalysts based on earth-abundant elements, such as Ni and Mo, that can be used for the conversion of lignin-derived compounds are desirable. However, they usually exhibit low activity and/or selectivity toward the target reaction, hydrodeoxygenation (HDO). For example, conversion of m-cresol in H2 over a typical Ni/SiO2 leads to ring hydrogenation at low temperatures and C-C hydrogenolysis to CH₄ at high temperatures. Here, we report that a bimetallic Ni−Mo/SiO₂ catalyst with Ni:Mo ratio ≈ 1 reduced at an optimized temperature can be very active and selective for HDO of m-cresol to toluene over a wide range of reaction temperatures (250-350 °C) and 1 atm of H₂. This behavior is explained in terms of the surface structure of Mo



oxides on the surface of Ni nanoparticles. Detailed characterization (XRD, Raman, TPR, EXAFS, and XPS) indicates that, after calcination, NiMoO4 is the predominant phase. However, after subsequent reduction, metallic Ni nanoparticles segregate out of the partially reduced MoO... Interestingly, while no significant structural/electronic modifications are detected for the bulk of the metallic Ni particles, the surface chemistry is clearly altered (i.e., no hydrogenolysis/hydrogenation, weak CO/H₂ adsorption, and lower electron density in the d band of Ni). These results suggest that after reduction, in contrast to the formation of NiMo alloy, the Ni surface gets decorated by reduced MoO_x moieties, a phenomenon similar to that previously observed on reducible oxides (so-called SMSI), which is essential for maximizing HDO and inhibiting hydrogenolysis.

KEYWORDS: m-cresol, hydrodeoxygenation, Ni, MoOx, modified Ni, C-C hydrogenolysis, SMSI

■ INTRODUCTION

Hydrodeoxygenation (HDO) is one of the key steps to upgrade lignin-derived bio-oils (mainly phenolics) to hydrocarbons that are compatible with petroleum-derived fuels. 1-4 HDO includes a series of reactions, i.e., deoxygenation, hydrogenation, hydrogenolysis, dehydration, and transalkylation, depending on the reaction conditions and catalysts employed. 5-9 The development of HDO catalysts based on earth-abundant elements as well as selective control of the deoxygenation reaction, with minimum H2 consumption, are two particularly appealing goals. Liquid-phase conversion of phenolics usually requires high H₂ pressures (>1 MPa), making the phenyl ring hydrogenation-dehydration a major pathway to remove oxygen. 10-12 By contrast, gas-phase conversion at low H₂ pressures (~0.1 MPa) could selectively deoxygenate phenolics to aromatics but normally high temperatures (>300 °C) are required. 13-15 Several types of catalysts have been investigated in recent years, including sulfide (e.g., NiMoS, CoMoS)^{16,17} and unsulfided (e.g., Fe/SiO₂, MoO₃, NiCu, etc.), 12-14 basemetal catalysts, as well as noble-metal catalysts (e.g., Pt/HBeta, Ru/TiO₂, etc.).¹⁸⁻²¹

Previous studies on gas-phase conversion over non-noble metal catalysts have shown some level of selective control of the deoxygenation reaction. 14,22,23 For example, Dufour et al. showed that Fe/SiO₂ exhibits a good selectivity (38%) for benzene, toluene, and xylene from HDO of guaiacol at 673 K and 1 bar H₂.¹³ Similarly, Román-Leshkov et al. reported that MoO₃ could selectively deoxygenate m-cresol and anisole to aromatics at >320 °C and <1 bar H_2 . ^{14,23} However, these catalysts mostly operate at high temperatures, with relatively low intrinsic activity and significant deactivation, mainly due to the modest ability of these metals to dissociate H₂ and hydrogenate surface carbon fragments. In this respect, Ni appears as a promising component for a HDO catalyst.

Received: March 28, 2019 Revised: June 12, 2019 Published: July 17, 2019



[†]Collaborative Innovation Center of Chemical Science and Engineering, School of Chemical Engineering and Technology, Tianjin University, Tianjin 300072, China

[‡]School of Chemical, Biological, and Materials Engineering, The University of Oklahoma, Norman, Oklahoma 73019, United States [§]Davidson School of Chemical Engineering, Purdue University, West Lafayette, Indiana 47907, United States

However, it typically exhibits a high propensity for phenyl-ring hydrogenation at low temperatures and C–C bond cleavage via hydrogenolysis at high temperatures, 24 which results in unacceptable carbon losses in the liquid range. Modification of Ni catalysts is of great interest to improve the Ni HDO performance. For instance, decreasing the Ni particle size is a way to reduce C–C hydrogenolysis over Ni. However, the Ni/SiO2 with a Ni particle size of 2 nm still shows >10% selectivity to CH4 at $\sim\!6\%$ m-cresol conversion at 350 °C and 1 atm H2. In addition, alloying Ni with Fe, Co, Re, etc., or modifying the Ni electronic state, e.g., by surface C deposition, could improve selective deoxygenation, but one could not expect that electronic interactions alone could inhibit C–C hydrogenolysis completely. $^{26-30}$

Here, we report the superior HDO performance of a bimetallic Ni–Mo/SiO $_2$ with equimolar Ni:Mo ratio when reduced at high temperatures. This catalyst not only shows 10-20-fold higher m-cresol HDO rates than monometallic Ni/SiO $_2$ or Mo/SiO $_2$ catalysts under same conditions, but also displays high deoxygenation selectivity (>80%) to toluene in a broad temperature range (250–350 °C). Specifically, it essentially shows no C–C hydrogenolysis to CH $_4$, even at 350 °C and 1 atm H $_2$, and less than 5% selectivity to phenyl ring hydrogenation at 250 °C and 1 atm H $_2$.

It should be noted that a few previous studies on the HDO of phenolics over NiMo bimetallic catalysts have been reported, with particular attention to the liquid-phase reaction. Addition of a promoter like S, P, and Mg or use of functional supports like CeO₂, ZrO₂, and Al₂O₃ have also been investigated. ^{16,31–37} For instance, Smirnov et al. proposed that bulk NiMoO_x could be completely reduced to metallic Ni, Mo, and NiMo alloy at 750 °C, which resulted in high activity for anisole ring hydrogenation in undecane at 300 °C and 6 MPa H₂. ³⁴ Lin et al. suggested that, for *p*-cresol conversion in *n*-hexadecane at 250 °C and 1 MPa H₂, the moderate oxophilicity of Mo promoted Ni and maximized toluene selectivity but only 25% compared with W and Fe. ³⁵

In this work, the relationship between the specific structure of a high-temperature reduced Ni-Mo/SiO₂ catalyst and their catalytic performance has been studied, combining m-cresol conversion measurements with a detailed characterization. A strong interaction between Ni and Mo has been observed after the initial calcination, followed by a more unique transformation during high-temperature reduction. Specifically, under the optimized reducing conditions (500 °C), the initially formed NiMoO₄ (particle size ≈ 3 nm) reduces to metallic Ni nanoparticles, which segregate out of the MoO_x matrix that remains as a partially reduced oxide. While Ni is fully reduced to the metallic state, the surface of these Ni nanoparticles remains sterically and chemically modified by surface MoO_x moieties, which we propose are responsible for the exceptional activity and selectivity displayed by this catalyst. An optimum is found for an equimolar ratio of Mo/Ni in which the two metals are initially forming NiMoO₄. Below this value a fraction of Ni remains as a separate oxide during calcination and cannot be modified by Mo during reduction, behaving like regular Ni with high C-C hydrogenolysis and hydrogenation activity. Above the equimolar Mo/Ni ratio, Ni sites seem to be excessively covered by MoO_x species, inhibiting H₂ activation and lowering the deoxygenation activity.

■ EXPERIMENTAL SECTION

Catalyst Preparation. The bimetallic Ni–Mo/SiO $_2$ catalysts were prepared by incipient wetness coimpregnation, as described before. The Ni and Mo precursors were Ni(NO $_3$) $_2$ ·6H $_2$ O (Strem Chemicals) and (NH $_4$) $_6$ Mo $_7$ O $_2$ 4·4H $_2$ O (Aldrich), respectively. After impregnation the samples were dried overnight at 120 °C, followed by calcination at 400 °C for 4 h. The Ni loading was fixed at 5 wt %, while Mo loading was varied to obtain the desired Mo/Ni molar ratios (0, 0.2, 0.5, 1, and 2) (Table S1). The bimetallic catalysts are denoted as NiMo51, NiMo21, NiMo11, and NiMo12, respectively, in the form of NiMoXY, where X:Y represents the molar ratio of Ni to Mo. The monometallic Ni/SiO $_2$ and Mo/SiO $_2$ catalysts had the same molar loading. The catalyst powder was pressed, crushed, and sieved to 40–60 mesh for reaction.

Catalyst Characterization. The metal loadings were determined by inductively coupled plasma atomic emission spectroscopy (ICP-AES). The values obtained by this analysis corresponded very well with the nominal loadings for each sample (Table S1). Nitrogen adsorption was measured in an automatic Micrometrics Digisorb 2600 analyzer. X-ray diffraction (XRD) patterns of the catalyst samples were recorded on a Rigaku D/max 2500 diffractometer with a Cu $K\alpha$ radiation source (λ = 1.54056 A). The Raman spectra were obtained on a Renishaw Raman spectrometer with an Ar⁺ ion laser (532 nm) exciting light source. Transmission electron microscopy (TEM) was performed on a JEM 2010F field emission system operating at 200 kV.

The hydrogen temperature-programmed reduction ($H_2\text{-}TPR)$ was recorded on a Chemisorb 2750 (Micrometrics) equipped with a thermal conductivity detector. Prior to measurements, 40 mg of catalyst sample was loaded in a Utube quartz reactor and pretreated with flowing N_2 at 300 $^{\circ}\text{C}$ for 1 h. After the sample was cooled down to room temperature, the gas was switched to 10% H_2/Ar . The sample was heated to 800 $^{\circ}\text{C}$ at a rate of 10 $^{\circ}\text{C}/\text{min}$ after the signal was stabilized.

CO and oxygen chemisorption were measured in a microreactor system equipped with a Cirrus 200 mass spectrometer (MKS). A 100 mg amount catalyst was reduced at 500 °C for 1 h in flowing H₂, followed by He purging for another 30 min. For CO chemisorption, the sample was then cooled to room temperature. Pulses of 5% CO/He (100 μ L) were sent to the catalyst until a constant CO (m/z=28) peak area was reached. For oxygen chemisorption, after the reduction process, the sample was cooled to 350 °C. Pulses of 5% O₂/He (100 μ L) were sent to the catalyst until a constant O₂ (m/z=32) peak area was reached. It was assumed that each O₂ molecule saturated two oxygen vacancies.

The NH $_3$ temperature-programmed desorption (NH $_3$ -TPD) was conducted on the same system as that used for CO and O $_2$ chemisorption. In each run, a 100 mg amount of catalyst sample was reduced at 500 °C for 1 h and then flushed with flowing He for another 30 min. After the temperature was reduced to 50 °C, the sample was exposed to a stream of 2% NH $_3$ /He for 30 min and then flushed again with flowing He for another 30 min. Finally, the temperature was increased to 650 °C at a heating rate of 10 °C/min.

In situ X-ray absorption spectroscopy (XAS) experiments were performed at the 10-BM beamline at the Advanced Photon Source (APS) at Argonne National Laboratory. Measurements were performed at the Ni K (8.333 keV) and

Mo K (20.000 keV) edges for each sample. Samples were pressed into a stainless-steel sample holder and placed in a quartz tube sample cell. The cell was sealed and treated at 500°C in 3.5% H₂, cooled to room temperature in He, and then transferred to the beamline. The measurements were performed in transmission mode in fast scan from 250 eV below the edge to 550 eV above the edge, which took approximately 10 min per scan. The scan ranges at the Ni and Mo edges were 8132-9000 and 19 750-20 800 eV, respectively. The data were interpreted using WinXAS 3.1 software to find the coordination number (CN) and bond distance (R) using standard procedures. Feff6 was used to develop a model to fit these samples at the Ni K edge. Theoretical phase and amplitude files were created for Ni-Ni (CN = 12, R = 2.49 Å), Ni-Mo (CN = 1, R = 2.56 Å), and Ni–O (CN = 1, R = 2.09 Å) scattering pairs. The S_0^2 was calibrated by fitting the Ni foil and was found to be 0.77. A least-squared fit the first shell of r space was performed on the k^2 -weighted Fourier transform data over the range from 2.71 to 11.0 Å⁻¹ in each spectrum to fit the magnitude and imaginary components. At the Mo K edge, the XANES was used to determine to Mo (Mo⁰, Mo⁴⁺, Mo⁶⁺) species present.

X-ray photoelectron spectroscopy (XPS) measurements were recorded on a Physical Electronics PHI 5800 ESCA system equipped with an Al K α X-ray anode operated at 300 W and 15 kV. The base pressure of the main chamber was kept at about 1.0×10^{-8} Torr. The pass energy was set as 58.7 eV for all measurements. The spectra were referenced to C(1s) at a binding energy (BE) of 284.8 eV. The surface composition was estimated from the integrated intensities corrected by atomic sensitivity factors.

Catalytic Measurements. The vapor-phase conversion of m-cresol over the Ni, Mo, and NiMo catalysts was evaluated in a fixed-bed quartz tube reactor, as described in previous work.²⁸ Briefly, catalyst sample (40-60 mesh) was placed between two layers of quartz wool in the center of the reactor. The catalyst was first reduced at 500 °C for 1 h in flowing H2 and then cooled down to reaction temperature (250-350 °C). m-Cresol was fed using a syringe pump (KDS100, KD scientific) and vaporized before entering the reactor. All lines were heated at 230 °C to avoid any condensation. The H_2/m -cresol molar ratio was kept at 60 in all runs. The products were quantified online in a gas chromatograph (GC7890B, Agilent). The effluent was trapped by methanol in an ice-water bath, and its components were identified using gas chromatography-mass spectrometry (Shimadzu QP2010SE). Fresh sample was used for each space time (W/F, $g_{cat} g_{reactant}^{-1} h$). The conversion and yield are reported in mol_{carbon}%.

■ RESULTS AND DISCUSSION

m-Cresol Conversion. Figure 1 illustrates the differences in product evolution from *m*-cresol conversion observed over the equimolar NiMo11 catalyst compared to that over a pure Ni/SiO₂ catalyst at both high (350 °C) and low (250 °C) reaction temperatures. At 350 °C the initial major products over Ni/SiO₂ were phenol (Ph) and CH₄ with very low (<10%) selectivity to toluene (Tol) and benzene (Ben) (Figure 1a), which are the desirable HDO products. As the conversion increases, all of the aromatic products decrease while CH₄ becomes dominant, that is *m*-cresol initially undergoes demethylation to Ph and CH₄ with minimal deoxygenation to Tol and Ben. As the extent of reaction progresses, the three aromatic products are fully cracked to CH₄ (Figure S1).³⁸ By contrast, over NiMo11, Tol is the major product, with some

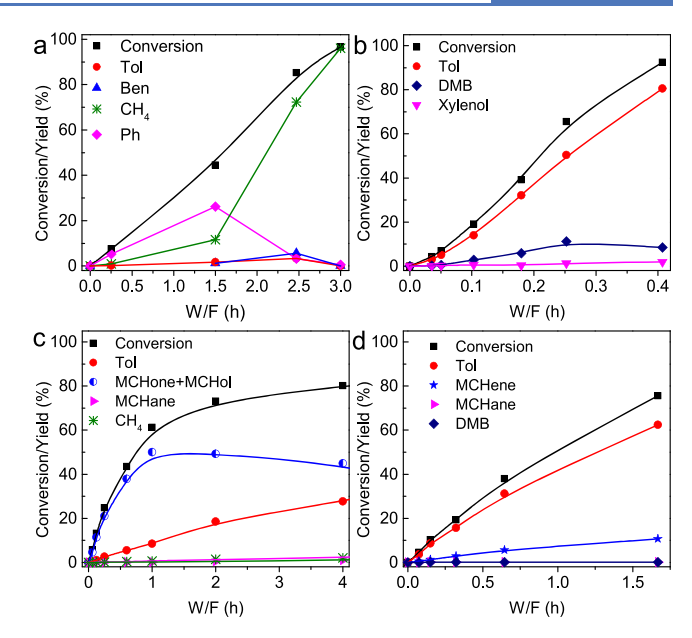


Figure 1. *m*-Cresol conversion and product distributions as a function of W/F over different catalysts and different reaction temperatures: (a) Ni/SiO₂, 350 °C; (b) NiMo11, 350 °C; (c) Ni/SiO2, 250 °C; (d) NiMo11, 250 °C. Reaction conditions: P = 1 atm, H_2/m -cresol = 60, TOS = 30 min.

formation of dimethyl biphenyl (DMB) (Figure 1b). Interestingly, no CH₄ is observed at any conversion level. Clearly, on this catalyst Ni has lost its characteristic high C–C hydrogenolysis activity, which is a remarkable result.

Likewise, at a low reaction temperature of 250 °C (Figure 1c), unmodified Ni effectively catalyzes the ring hydrogenation of m-cresol to 3-methylcyclohexanone (MCHone) and 3methylcyclohexanol (MCHol). However, under the same conditions, NiMo11 does not yield any MCHone or MCHol. On the contrary, it retains a very high selectivity to Tol, which appears to be the only primary product (see the low W/F region in Figure 1d). At higher W/F, small amounts of methylcyclohexene (MCHene) and methylcyclohexane (MCHane) are observed. Since MCHene is not formed when feeding Tol, it must come from a fast dehydration of small amounts of MCHol that may be formed. Interestingly, on unmodified Ni (Ni/SiO₂), no MCHene is observed since even if any amount of this olefin is produced it would be rapidly hydrogenated to MCHane. ^{38,39} Clearly, this does not occur on NiMo11, which further illustrates its unique behavior.

To rule out the possibility that Tol is not a primary product but arises from ring hydrogenation of *m*-cresol to MCHol followed by dehydration and further dehydrogenation to Tol, MCHol was fed under the same conditions (see results in Figure S2). In this case, it was found that indeed MCHol does dehydrate to MCHene, but no Tol was formed, which shows that the indirect hydrogenation—dehydration—dehydrogenation path is not responsible for the HDO of *m*-cresol over NiMo11 at 250 °C, but rather Tol is directly formed via direct C–O cleavage, demonstrating the high HDO activity and selectivity of this catalyst, even at mild temperatures. In addition, it is worth noting that MCHene hydrogenates to MCHane with an extremely low rate, a reaction that is very fast on unmodified Ni under these conditions. ^{38,39}

The effect of varying the Mo/Ni molar ratio on *m*-cresol conversion activity and Tol formation rate was studied at low

conversions at 350 °C, as shown in Figure 2a. It can be observed that the rates of *m*-cresol disappearance and Tol

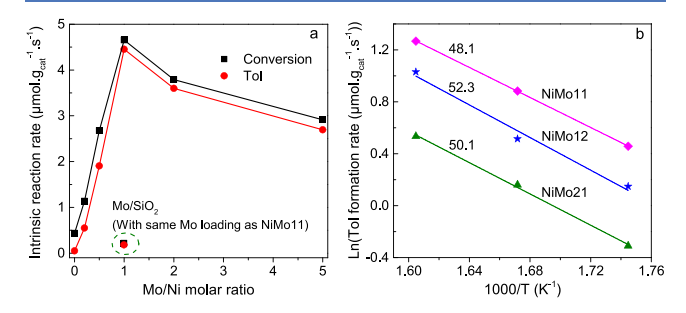


Figure 2. (a) Effect of Mo/Ni molar ratio on the intrinsic reaction rate of *m*-cresol conversion and Tol formation at 350 °C. (b) Arrhenius plots of *m*-cresol deoxygenation to Tol over NiMo catalysts with different Mo/Ni molar ratios at a temperature range of 300–350 °C. Number near the line shows the activation energy with units of kJ/mol. Reaction conditions: H_2/m -cresol = 60, P = 1 atm, TOS = 30 min. W/F was adjusted to achieve *m*-cresol conversion < 10%.

formation continuously increases with Mo/Ni ratio from 0.43 and 0.05 μ mol·g_{cat}⁻¹·s⁻¹, respectively, over pure Ni/SiO₂ to maximum values of 4.65 and 4.45 μ mol·g_{cat}⁻¹·s⁻¹, respectively, over the NiMo11 catalyst. Beyond this ratio the activity drops. A similar trend can also be observed over NiMo/SiO₂ catalysts with the same Mo loading and varying Ni loadings (Figures S3–S6). Moreover, the bimetallic NiMo11 catalyst is more than 23 times more active than the monometallic Mo/SiO₂ (Figure 2a), which shows that Mo alone is not responsible for the high HDO activity but rather both Ni and Mo sites are required. Interestingly, as shown in Figure 2b, all bimetallic NiMo catalysts exhibit similar HDO apparent activation energies (~50 kJ/mol), which indicates that all of these catalysts may have varying density of active sites but are all similar in nature. By contrast, the activation energy obtained for the Ni/SiO₂ is much higher (77 kJ/mol).²⁵

To further illustrate the unique behavior of the bimetallic catalysts at varying Mo/Ni ratios, we compared the extent of C-C hydrogenolysis to CH₄ at the same high m-cresol conversions (~95%) at 350 °C (Table S2). At this high conversion, the CH₄ selectivity is 100% over the pure Ni catalyst and sharply drops as the Mo/Ni ratio increases, which becomes totally inhibited for NiMo11 and NiMo12 catalysts. These results indicate that Mo species are responsible for inhibition of the hydrogenolysis activity of Ni, while the HDO activity requires the presence of both metals. Likewise, a comparison was made at 250 °C and lower *m*-cresol conversion levels (see Table S3). A similarly sharp decrease in the yield of ring hydrogenation products was observed with increasing Mo/ Ni ratio. Therefore, the level of residual C-C hydrogenolysis at high temperatures and ring hydrogenation at low temperatures can be taken as indicators for the presence of residual unmodified Ni left on the catalyst. To shed more light into the structure of this series of Ni-Mo catalysts, a detailed materials characterization was conducted before and after reduction in H₂.

Catalyst Structure after Calcination. Figure 3a shows the XRD patterns of the samples calcined in air at 400 $^{\circ}$ C for 4 h. As expected, the SiO₂-supported monometallic Mo and Ni catalysts exhibit the characteristic monoclinic MoO₃ and FCC NiO phases, respectively. The two NiMo samples with Mo/Ni molar ratio < 1 do not show any peaks associated with Mo

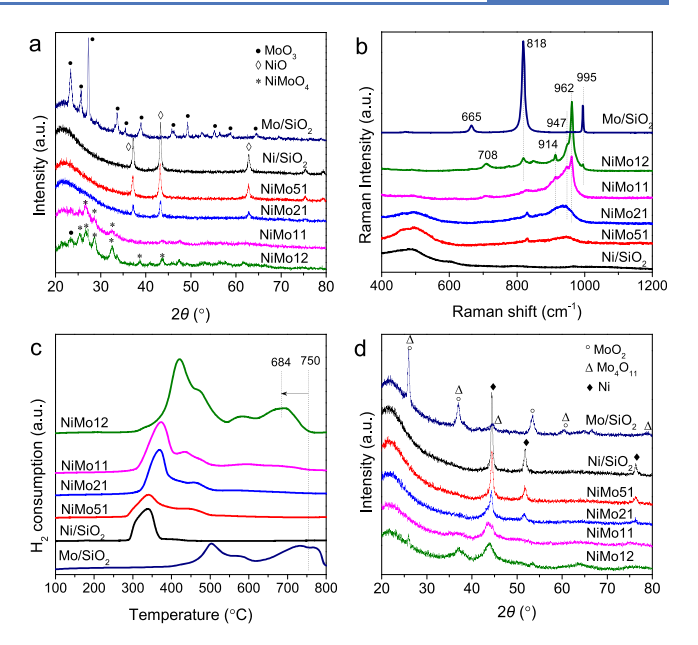


Figure 3. (a) XRD patterns of calcined catalysts. (b) Raman spectra of calcined catalysts. (c) H_2 -TPR profiles of calcined catalysts. (d) XRD patterns of catalysts reduced in H_2 at 500 °C.

species, which may be highly dispersed and undetectable by XRD. Apparently, the presence of NiO favors the dispersion of Mo. Similarly, the presence of Mo also decreases the intensity of NiO diffraction. The average particle sizes, calculated from the full width at half-maximum of NiO at $2\theta = 43.3^{\circ}$ by the Scherrer equation, are 23, 13, 8 nm for Ni, NiMo51, and NiMo21, respectively, indicating that the presence of Mo species also favors the dispersion of Ni. Interestingly, for the catalyst with the optimum HDO activity (NiMo11), neither MoO₃ nor NiO peaks were detected, but only some weak and broad diffraction peaks corresponding to the formation of NiMoO₄ are observed,³⁴ indicating that all of the Ni and Mo species in this catalyst participate in the formation of highly dispersed NiMoO₄. It is then expected that for the samples with Mo/Ni ratios < 1 most of the undetected Mo should exist as highly dispersed NiMoO₄ with the excess NiO forming larger aggregates, which are responsible for the NiO diffraction peaks detected in NiMo51 and NiMo21. Analogously, when Mo/Ni > 1, all of the Ni is in NiMoO₄ while the excess Mo is in the form of MoO₃, as detected in the NiMo12 and NiMo15 (Figure S7).

Raman spectroscopy was also conducted to further identify the nature of the oxide species present on the different catalysts after calcination, as shown in Figure 3b. First, Ni/SiO₂ shows weak Ni-O stretching bands at 550-500 cm⁻¹, 40 while Mo/ SiO₂ shows sharp and strong bands at 665, 818, and 995 cm⁻¹, which are characteristic of monoclinic MoO₃ crystals. 41,42 By contrast, NiMo11 displays clear bands at 708, 914, and 963 with a shoulder at 947 cm⁻¹, which are attributed to the ν_s (Ni–O–Mo), ν_a (Mo=O), and ν_s (Mo=O) vibrational modes of NiMoO₄ species, 43 in good agreement with the XRD observations. On the samples with Mo/Ni < 1, clear Ni-O stretching bands at 550-500 cm⁻¹ are observed, indicating the presence of NiO. Also, very weak and broad bands associated with NiMoO₄ can be observed, indicating that these NiMoO₄ species, not detected by XRD on these samples, are present in small amounts and a high state of dispersion. As expected, the NiO band disappears for NiMo11 and NiMo12, while clear

NiMoO₄ bands appear, supporting the proposal that all of the Ni is forming NiMoO₄. In addition, the NiMo12 sample, with Mo in excess, shows a small but clearly observable band at 995 cm⁻¹, characteristic of MoO₃. The low intensity of this band compared to that observed for the Mo/SiO₂ catalyst shows that indeed the excess MoO₃ moieties in NiMo12 are highly dispersed.

The interaction between Ni and Mo was further investigated by H2-TPR (Figure 3c). Ni/SiO2 displays a hydrogen consumption peak from 290 to 370 °C (Ni²⁺ to Ni⁰), 44 whereas Mo shows two reduction stages at much higher temperatures, one from 400 to 620 °C (attributed to the reduction of Mo⁶⁺ to Mo⁴⁺) and the other from 620 to 800 °C (Mo⁴⁺ to Mo⁰).⁴⁵ By contrast, the bimetallic NiMo catalysts show very different reduction behavior from either Ni/SiO2 or Mo/SiO₂, indicating the strong interaction between Ni and Mo. On the NiMo catalysts, the first TPR peaks, attributed to the reduction of Ni oxide species, appear shifted to higher temperatures. This shift is a clear fingerprint for a direct interaction between Ni and Mo. As proposed for the reduction of CoMo catalysts, 46 polarization of Ni-O bonds, caused by the presence of nearby Mo⁶⁺, which makes them more ionic, may be responsible for the observed hindrance in Ni reducibility. The reduction process for NiMo catalysts with Mo/Ni \leq 1 starts at ~290 °C and essentially ends at ~500 °C. The H₂ consumption peaks at higher temperature, which are dominant for the Mo/SiO2 catalyst, are very small for these catalysts, which shows that most of the Mo species are in the form of NiMoO₄ rather than MoO₃, as previously concluded from the XRD and Raman data. For the NiMo12 catalyst, with a higher Mo loading, the low-temperature reduction process (300-540 °C) should also be ascribed to the reduction of NiMoO₄, whereas the other higher temperature reduction process (540-760 °C) is a clear indication of the presence of excess MoO₃. Note that the reduction of this excess MoO₃ ends at a significantly lower temperature than the MoO₃ in the Mo/ SiO₂ catalyst (Figure 3c). As inferred from XRD and Raman, this excess MoO₃ is interacting with NiMoO₄ species, which facilitates its reduction.

Quantification of the TPR results (Table S4) shows that the molar ratio of H₂ consumption to Ni (H₂/Ni) for Ni/SiO₂ is 0.99, indicative of complete reduction of NiO. In contrast, the H₂/Mo consumption ratio is 2.5 for Mo/SiO₂. Similar H₂/Mo ratio values of 2.0-2.5 are obtained for bimetallic NiMo catalysts when assuming complete reduction of Ni. As indicated by XRD and Raman, the Mo oxide species before reduction are MoO₃ and NiMoO₄. Both of them require a H₂/Mo consumption ratio of 3 for complete reduction to metallic Mo. Accordingly, the difference in actual and maximum H₂/Mo ratios can be used to determine the extent of Mo reduction. A reduction temperature of 500 °C before reaction was chosen because it resulted in the highest activity (Figure S8). At this reduction temperature, assuming 100% reduction of Ni²⁺ to Ni, the remaining H2 consumption corresponds to a reduction of the original Mo⁶⁺ to an average oxidation state Mo^{3,3+} for the bimetallic NiMo catalysts but only Mo^{5.2+} for Mo/SiO₂ (Table

On the basis of the above characterization results, Figure 4a depicts a simplified schematic structure of the different catalysts after calcination. On monometallic catalysts, Ni and Mo species tend to aggregate into large particles on the support due to the weak interaction of silica with either NiO or MoO_3 . By contrast, on the bimetallic catalysts, this weak interaction with the

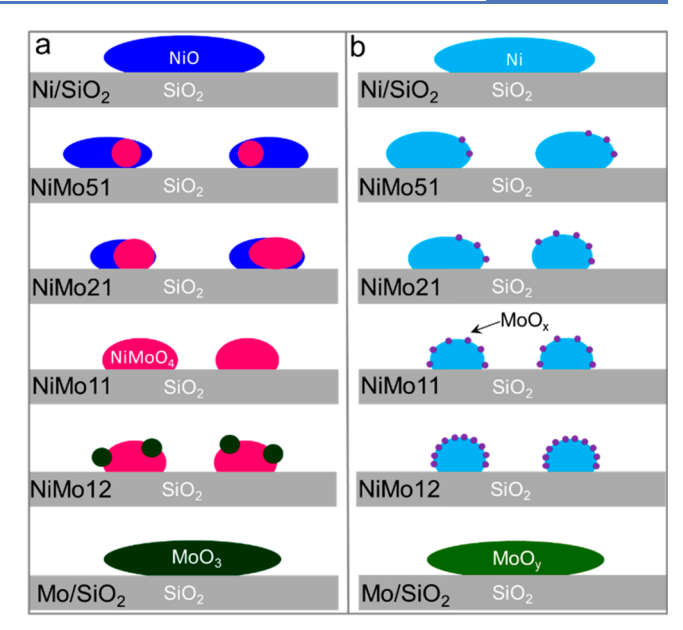


Figure 4. Schematic structure of catalysts phases after (a) calcination in air at 400 °C, which include NiO (blue), NiMoO₄ (red), ad MoO₃ (olive) over the SiO₂ support and (b) reduction in H₂ at 500 °C, which include metallic Ni (light blue), MoO_x moieties (purple), and MoO_y (green), with x < y.

support facilitates the Mo and Ni species to interact more strongly, forming bimetallic NiMoO₄. When the Mo/Ni molar ratio = 1, all of the Ni and Mo are combined to form NiMoO₄. Above or below this ratio, either MoO₃ or NiO, respectively, exists in excess.

Catalyst Structure after Reduction. Figure 3d shows the XRD patterns of catalysts after ex-situ reduction at 500 °C in $\rm H_2$ for 1 h followed by passivation in air. Only metallic Ni was detected for the Ni/SiO₂ sample, whereas a combination of different Mo oxide species like MoO₂ and Mo₄O₁₁ was detected over Mo/SiO₂. In the bimetallic NiMo samples with Mo/Ni ≤ 1, for which all of the Mo was present as highly dispersed NiMoO₄ after calcination, no Mo oxide was detected by XRD after reduction. At the same time, a drastic reduction in intensity was observed for the Ni diffraction peaks, indicating that the interaction with Mo improves the Ni dispersion. By contrast, for the NiMo12 sample, with excess Mo, a clear diffraction peak is observed at 26.0°, corresponding to suboxides MoO₂ or Mo₄O₁₁, resulting from reduction of the excess MoO₃.

TEM (Figure S9) supports the notion that a higher Mo/Ni ratio reduces the Ni particle size. Specifically, the observed average particle sizes are 5.0, 3.1, and 3.3 nm for NiMo21, NiMo11, and NiMo12 samples, respectively.

To further investigate the structure of the catalysts after reduction in $\rm H_2$ at 500 °C we conducted in situ X-ray absorption, analyzing both Ni and Mo K edges. The oxidation state of the Ni in each catalyst was determined by the X-ray absorption near-edge structure (XANES), Figure 5a. Clearly, the Ni XANES energy, shape, and white line for all Ni/SiO₂ and NiMo catalysts closely resemble that of the Ni foil, indicating a full reduction of NiO or NiMoO₄ to Ni nanoparticles. Similarly, the Ni magnitude of the k^2 -weighted Fourier transform (FT), Figure 5b, for different catalysts shows that the position of the peak and shape of the imaginary part (not shown) match that of metallic Ni foil with no evidence of unreduced Ni–O

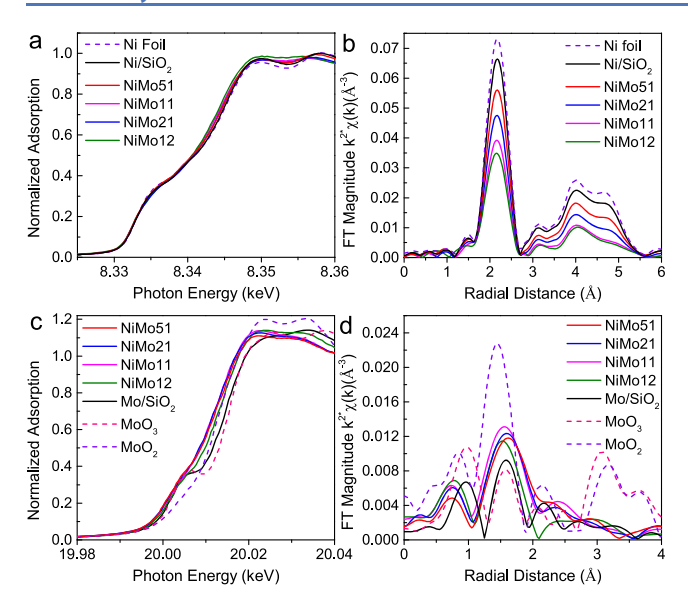


Figure 5. (a) Normalized XANES at the Ni K edge. (b) Ni magnitude of Fourier transform of the k^2 -weighted EXAFS spectra. (c) Normalized XANES at the Mo K edge. (d) Mo magnitude of the Fourier transform of the k^2 -weighted EXAFS spectra of in-situ-reduced catalysts, $\Delta k = 3.0-12.2$ Å. Reference samples of metal Ni foil, MoO₂, and MoO₃ are shown with the dashed lines.

scattering. As the Mo loading increases, the magnitude of the FT becomes smaller, indicating a lower Ni–Ni coordination number, in agreement with the XRD observations. Moreover, analysis of the EXAFS data shows that good fits can be obtained for all catalysts by only using a Ni–Ni scattering path without adding any Ni–Mo bond contribution (Table 1 and Figure

Table 1. EXAFS Fitting Parameters over a Fourier Transform Range from 2.7 to 11 ${\rm \AA}^{-1}$ at the Ni K Edge for the Ni–Ni Scattering Path

sample	XANES energy (keV)	CN ^a	$R (Å)^a$	σ^2 $(\mathring{A}^2)^a$	$\frac{\Delta E}{(eV)^a}$	d (nm) ^b
Ni/SiO ₂	8.333	10.6	2.49	0.005	5.4	9.4
NiMo51	8.333	9.0	2.49	0.005	4.9	6.4
NiMo21	8.333	7.7	2.49	0.005	4.2	4.2
NiMo11	8.333	6.3	2.49	0.005	3.2	3.1
NiMo12	8.333	5.7	2.49	0.005	2.3	2.1

^aThe error of all of the fitted parameters are very similar between different samples. The average error in CN (coordination number) is 0.2, in r (bond length) is 0.003 Å, in ΔE_0 (energy shift) is 0.5 eV, and in σ (Debye–Waller factor) is 0.005 Å. ^bThe Ni particle size was estimated using the correlations developed for Au nanoparticles which follows the equation log $(100/d) = -0.130 \cdot \text{CN} + 2.58.47$.

S11). In fact, inclusion of a Ni–Mo scattering path leads to poorer fits, indicating that no metallic Mo is present in the Ni nanoparticles, which is also consistent with the XANES spectra. The Ni particle sizes estimated from the coordination number⁴⁷ are included in Table 1. They show a similar trend as those obtained from XRD and TEM, that is, the Ni dispersion increases with the Mo/Ni ratio.

The Mo K edge was also studied by XANES, Figure 5c. As the oxidation state increases from Mo^0 (Mo foil) to Mo^{4+} (MoO_2) and Mo^{6+} (MoO_3), the XANES energy increases to higher values (Figure S12). In addition, there is a pre-edge feature that characterizes Mo^{6+} . Accordingly, the spectrum of

the Mo/SiO₂ sample closely resembles that of the MoO₃ reference, indicating that it contains predominantly Mo⁶⁺. It is observed that the addition of Ni leads to subtle changes in the energy and shape of the Mo XANES. This is predominantly due to partial reduction of Mo⁶⁺ to Mo⁴⁺, in accordance with the TPR results. A linear combination XANES fit between MoO₂ and MoO₃ gives the approximate fractions of Mo⁴⁺ and Mo⁶⁺ (Table S6). Addition of Ni leads to a slight increase in the amount of reduced Mo⁴⁺ in the bimetallic NiMo catalyst compared to Mo/SiO₂. The Mo EXAFS, Figure 5d, shows changes in Mo-O coordination geometry. Due to the complexity of the spectra, these could not be fit; however, they do show the absence of Ni-Mo bonding, indicating that a Ni-Mo alloy is not formed, as concluded above from the Ni edge analysis. In summary, the reduced catalysts contain a combination of metallic Ni nanoparticles and MoO_x (predominantly Mo⁴⁺ in NiMo samples), but there is no evidence of a bimetallic Ni-Mo alloy.

Therefore, both XANES and EXAFS show no significant electronic modification of Ni in the bimetallic NiMo catalysts compared to Ni/SiO₂. However, XAS is a bulk technique, not sensitive to potential electronic changes if they only occur on the surface of the particles. In fact, the observed reactivity of the reduced catalyst indicates that the surface properties of Ni are drastically altered, losing the intrinsic properties of normal Ni. Consequently, to investigate the possibility of any chemical modification on the surface, we used two surface-sensitive techniques, CO chemisorption and XPS, which can probe this modification.

As shown in Figure 6, it is observed that Mo/SiO₂ does not show any CO adsorption at room temperature. When a series of

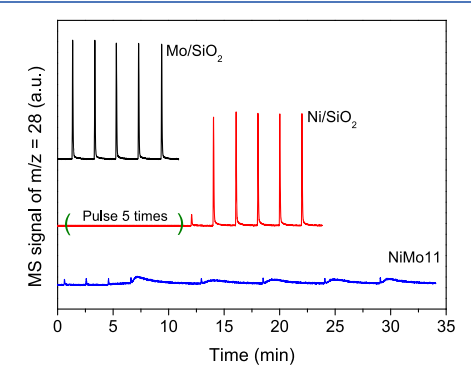


Figure 6. CO pulse adsorption profiles over Mo/SiO₂, Ni/SiO₂, and NiMol1 at room temperature.

consecutive CO pulses was sent through the catalyst bed, the CO intensity did not change. By contrast, for Ni/SiO₂ the first 5 pulses of CO were completely adsorbed by the sample, while the surface became saturated after the sixth pulse. Interestingly, the reduced NiMo11 catalyst exhibited a different behavior from the monometallic catalysts, evidenced by the very different shape of the pulses, which can be interpreted as a weak adsorption followed by immediate desorption. This modification of the Ni–CO interaction reflects a strong interaction of Ni with MoO_x. Since the in situ XAS analysis excluded any bulk electronic modification of Ni or formation of a Ni–Mo alloy, it can be concluded that a local surface modification is responsible for the observed drastic changes in chemisorption. This is reminiscent of the weak CO adsorption observed on samples affected by the so-called SMSI effect, ^{48–50} which was explained

by migration of TiO_x (or other reducible oxides) species over Group VIII metal catalysts. 50-53 Another characteristic feature of TiO₂-supported catalysts in the SMSI state is the loss of C-C hydrogenolysis, similar to that observed in our NiMo catalyst, that is, the operational definition for SMSI was the suppression of H₂ and CO chemisorption and the loss of activity for structure-sensitive reactions such as C-C hydrogenolysis that require an ensemble of metal atoms. In that sense, the hightemperature reduced NiMo catalyst perfectly matches the SMSI behavior. 48 In addition, according to Figure S8, a reduction temperature of 500 °C is essential to maximize the deoxygenation activity, whereas after more severe reduction (550 °C or above), at conditions where NiMo alloy may be formed, 34,54 the HDO activity drops, indicating that the presence of a NiMo alloy is not required for HDO. By contrast, a MoO_x-modified Ni surface seems to be the actual required site for deoxygenation. Interestingly, a very selective catalyst can also be obtained by directly depositing NiO on MoO₃. As shown in Figure S13, the NiO particle size is about 26 nm, similar to that on the Ni/SiO2 catalyst. However, after reduction at 500 °C, contrary to the HDO behaver of Ni/ SiO2, this Ni/MoO3 catalyst shows high deoxygenation selectivity to toluene and very low C-C hydrogenolysis selectivity to CH₄ and Ph (Table S7), indicating a complete modification of the Ni properties. With such a large particle size of Ni, the only conceivable modification of the surface is via a decoration by MoO, species, a SMSI-like phenomenon.

Moreover, two possible interpretations can be offered to explain the weaker CO–Ni interaction in the bimetallic catalysts. First, an electronic interaction between surface Ni and MoO_x species may alter the electron density of Ni, thus weakening the adsorption of CO. Second, a weaker CO adsorption may not necessarily imply a chemical perturbation of the metal surface, since it has been proposed that simple geometric blockage of sites may affect the structure of adsorbed CO from a more strongly bound to a less strongly bound mode. St

XPS was then performed to probe any possible electronic interaction between Ni and surface MoO_x species. Figure 7a shows the Ni 2p spectra with the corresponding deconvoluted

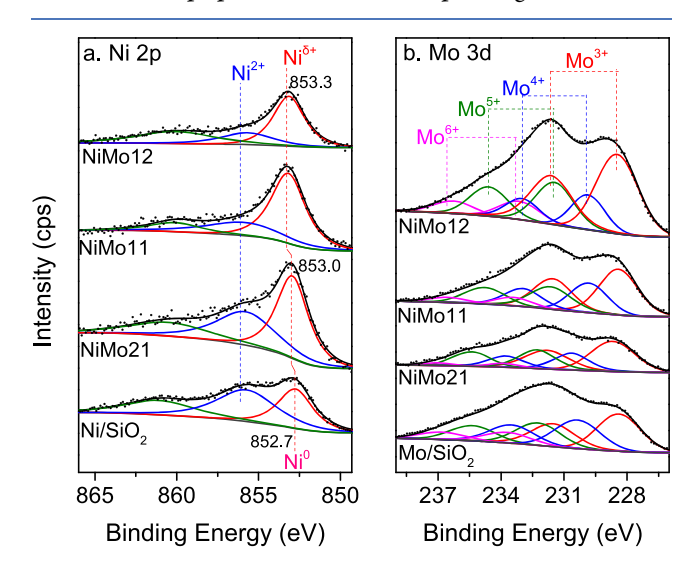


Figure 7. XPS spectra of (a) Ni 2p and (b) Mo 3d. Dots, experimental data; lines, curve fittings. Samples were prereduced ex situ at 500 °C for 1 h.

peaks for each sample. The deconvoluted peaks centered at 852.7, 855.8(± 0.1), and $\sim 860.8(\pm 0.2)$ eV are assigned to Ni⁰, Ni²⁺, and its shakeup satellite peak, respectively.²⁸ It should be noted that the sample was reduced ex situ and transferred to an airtight glovebag before entering the XPS unit and a small extent of surface oxidation occurred, which explains the presence of the observed Ni²⁺ species. In comparison with the Ni/SiO₂ sample centered at 852.7 eV for Ni⁰, the binding energy (BE) of Ni⁰ 2p_{3/2} shifts to a higher BE at 853.0 eV for the NiMo21 and even higher at 853.3 eV for NiMo11 and NiMo12 samples. These clear shifts to higher BE can be assigned to an electron transfer from the metallic Ni to surface MoO_x species. It suggests the chemical modification of the Ni surface by MoO_x, in accordance with the weaker CO adsorption on NiMo catalyst than that on Ni/SiO₂.

Figure 7b compares the Mo 3d spectra of NiMo catalyst with that of Mo/SiO_2 . Deconvolution of the peaks shows a mixture of different oxidation states (Mo^{3+} , Mo^{4+} , Mo^{5+} , and Mo^{6+}) for each sample. Clearly, the Mo/SiO_2 catalyst shows a much lower amount of Mo^{3+} as well as higher amounts of Mo^{4+} and Mo^{6+} compared with the bimetallic NiMo samples, indicating that Ni promotes the reduction of Mo oxide (Table 2), in accordance with the H_2 -TPR and XANES results.

As shown in Table 2, the surface Ni/Si ratio increases almost 2-fold from 0.010 (for Ni/SiO₂) to 0.019 (for NiMo21), indicating a higher Ni dispersion of NiMo21 than Ni/SiO2. However, NiMo11 shows a slightly lower Ni/Si ratio (0.016). Further increase in Mo loading (for NiMo12) shows a significant decrease in the Ni/Si ratio to 0.009, while all of the bulk characterization techniques show that the Ni dispersion increases with Mo loading. The lower surface Ni/ Si ratio at higher Mo loadings can be explained by the proposed SMSI structure, that a large fraction of the Ni surface is covered by MoO, species. Moreover, a clear trend is observed in the extent of Ni oxidation by air exposure as a function of Mo/Ni ratio. A large fraction of Ni is oxidized in the Ni/SiO2 catalyst, whereas the oxidation occurs at a much lower extent on the bimetallic catalysts. This trend supports the concept of MoO_x covering and chemical modification on Ni, making it less oxophilic. In addition, both the Mo/Si and the Mo/Ni ratios increase with increasing Mo loadings. Note that the XPS Mo/ Ni ratio (0.58, 1.13, and 2.96) consistently exceeds the theoretical bulk ratios (0.5, 1, and 2) for each sample, which is also consistent with Mo species partially covering the Ni surface, as proposed.

To obtain a direct observation of the proposed SMSI structure, we conducted HRTEM on the bimetallic NiMo21 catalyst, since it has both large and small particles (Figure S9), making it easier to examine the fine structure. Figure 8a shows the image of a large Ni particle with lattice fringes of 0.205 and 0.180 nm, corresponding to Ni(111) and Ni(200) spacings, respectively. Interestingly, a thin amorphous layer is observed partially covering this Ni particle. We speculate that this layer might be the highly dispersed MoO_x species proposed above. In addition, some small crystalline clusters with lattice fringes of 0.235 nm were observed at the edge of the Ni particle. This large spacing does not correspond to any of the planes of metallic Ni, which we ascribe to MoO_x. Similar analysis was performed with smaller Ni particles on the same sample. Some thin amorphous layers (MoO_x) at the edge of Ni particle may also be present along with fringes of metallic Ni (Figure S14). Additionally, energy-dispersive X-ray spectroscopy (EDS) elemental mapping further demonstrates a rather uniform

Table 2. Distribution of Different	Valence States of Ni and Mo as	Well as Atomic Ratios Derived from XPS

	distribution of valence states (%)								
	Ni		Mo			atomic ratio			
catalyst	Ni ⁰	Ni ²⁺	Mo ³⁺	Mo ⁴⁺	Mo ⁵⁺	Mo ⁶⁺	Ni/Si	Mo/Si	Mo/Ni
Ni/SiO ₂	42.5	57.5					0.010		
NiMo21	57.1	42.9	45.5	23.2	27.3	4.0	0.019	0.011	0.58
NiMo11	71.2	28.8	44.0	25.6	23.4	7.1	0.016	0.018	1.13
NiMo12	72.8	27.2	44.5	15.7	29.8	10.0	0.009	0.027	2.96
Mo/SiO_2			36.4	29.1	22.8	11.6		0.017	

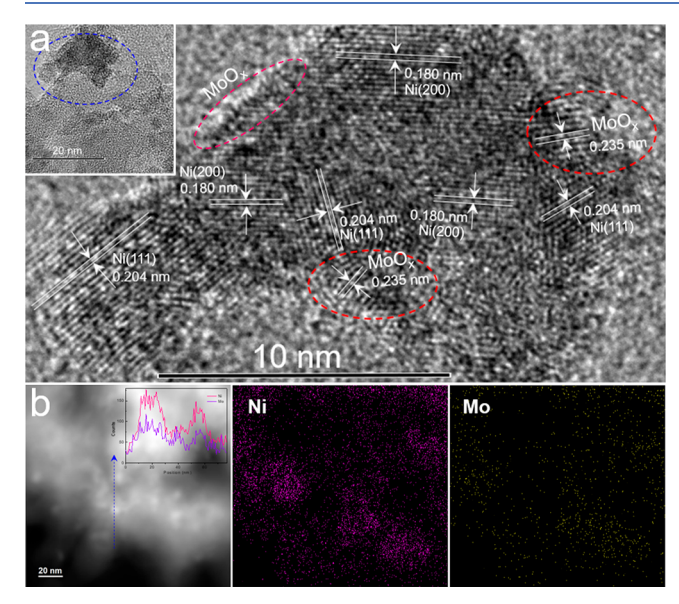


Figure 8. (a) HRTEM image of NiMo21 with a insert showing TEM image in a large area. (b) HAADF-STEM image with line scanning and dot scanning, and EDS mapping of Ni and Mo elements of NiMo21.

distribution of Mo on the Ni particles for both NiMo21 (Figure 8b) and NiMo11 (Figure S15) samples. Moreover, line-scanning EDS (see insets) along the blue line in Figure 8b demonstrates the intimate interaction between Ni and Mo species. Clearly, the Mo/Ni ratio is higher at the edge than at the center of the particles, suggesting that Mo is preferentially located at the external surface of the Ni particles, which once again is consistent with the concept of a SMSI-like structure.

On the basis of the above analysis, we propose the schematic structure of different catalysts after reduction in H2 at 500 °C (Figure 4b), that is, we have shown that NiO reduces to metallic Ni over Ni/SiO2. While NiMoO4 in NiMo catalysts also reduces to a metallic Ni core, the surface of Ni remains partially decorated with MoO_x moieties, which sterically and chemically modified the Ni surface. When Mo/Ni < 1 (NiMo51 and NiMo21), the excess Ni retains its original properties, i.e., C-C hydrogenolysis at 350 °C and phenyl ring hydrogenation at 250 °C during m-cresol HDO (Tables S2 and S3). However, when Mo/Ni > 1, MoO_x covers the Ni surface to a high extent. While it eliminates the intrinsic properties of Ni (hydrogenolysis and hydrogenation), it also blocks access to Ni and lowers the overall HDO activity. The Mo/Ni = 1 (NiMo11) with optimum surface MoO_x coverage not only has a low hydrogenolysis and hydrogenation activity but also maximum deoxygenation activity.

It is known that decreasing Ni particle size results in enhanced HDO selectivity with inhibited C-C hydrogenolysis.²⁵ However, particle size effects alone cannot be

responsible for the drastic effects observed here on the NiMo bimetallic catalyst series. In the previous study, $^{2.5}$ even when the Ni particle size was reduced to 2 nm for a monometallic Ni/SiO₂ catalyst, the selectivity to CH₄ at 350 °C was higher than 10%, even at a low *m*-cresol conversion of 6%, that is, regardless of the particle size, unmodified Ni keeps its intrinsic properties, with preference toward C–C hydrogenolysis at high temperatures and phenyl ring hydrogenation at low temperatures. Only with the presence of MoO_x moieties on the surface, it is possible to completely eliminate these side reactions and maximize HDO selectivity.

O vacancies have also been proposed to be the active deoxygenation sites for HDO of m-cresol over Mo/SiO₂. ²³ As shown in Table S1, the same reduction treatment creates twice as many O vacancies on the bimetallic NiMo11 than on the monometallic Mo/SiO₂ catalyst with same Mo loadings, clearly related to the higher dispersion and reducibility of Mo species on NiMo11. In line with this, the density of exposed cations (Lewis acid sites), quantified by NH3-TPD (Figure S16 and Table S1), was found to be proportional to the loading of Mo sites, with NiMo11 and Mo/SiO2 samples having a similar amount of acid sites, which is \sim 10 times higher than that in Ni/ SiO₂. Interestingly, the density of these sites correlates well with the activity of acid-catalyzed reactions, such as MCHol dehydration (Figure S17), but not with HDO (Figure S18), for which the simultaneous presence of both Ni and Mo in close proximity seems to be essential.

It is important to differentiate the behavior of the bimetallic NiMo catalyst with that of MoO₃. For example, on the latter, the deoxygenation activity has shown an induction period when the activity is measured as a function of time on stream (TOS) during the HDO of m-cresol at 300-350 °C and 1 atm H₂. It has been shown that in that case the most active site seems to be a partially carburized oxycarbide phase. 14,55 By contrast, no induction period was ever observed with the NiMo catalysts, and essentially no formation of a carbide or oxycarbide phase was observed by XRD on this catalyst after reaction (Figure S19). Furthermore, when carburization was deliberately brought about by pre-exposing the catalyst to cresol at 350 °C for 80 min, the subsequently measured activity was significantly lower (Figure S20). Thus, we have shown that the Mo species alone are not enough to achieve the high deoxygenation activity exhibited by the reduced NiMo catalysts. Both the presence of Ni at an optimum Mo/Ni ratio and an appropriate reduction temperature (500 °C) maximize the activity and selectivity.

CONCLUSION

We report here a highly active and selective HDO catalyst, i.e., 5 wt %Ni-8.2 wt %Mo/SiO₂ (Mo/Ni molar ratio = 1), comprising a highly dispersed Ni core decorated with MoO_x

which sterically and chemically modify its surface. This material shows high m-cresol HDO activity at 350 °C and 1 atm H₂, which is more than an order of magnitude higher than those of monometallic Ni/SiO₂ and Mo/SiO₂ catalysts. Moreover, the selectivity toward the desired HDO product (toluene) at both high (350 °C) and low (250 °C) reaction temperatures is higher than most catalysts previously reported. More importantly, it shows no C-C hydrogenolysis activity, even at a high reaction temperature (350 °C), compared to 100% selectivity to CH₄ exhibited by Ni/SiO₂. The synergistic cooperation between the Ni core surface and optimum amounts of MoO_x species decorating the Ni surface are important to achieve high activity and selectivity. When Mo/Ni molar ratio < 1, some Ni surface remains unmodified by MoO, species and behaves like monometallic Ni/SiO2, with significant C-C hydrogenolysis activity at 350 °C and phenyl ring hydrogenation activity at 250 °C; whereas when Mo/Ni > 1, the surface of the Ni particles becomes excessively covered with MoO_x species, which inhibits H₂ activation and lowers the deoxygenation activity.

ASSOCIATED CONTENT

S Supporting Information

The Supporting Information is available free of charge on the ACS Publications website at DOI: 10.1021/acscatal.9b01285.

Basic catalysts information, reaction scheme, product distribution at 350 and 250 $^{\circ}$ C, 3-methycyclohexanol dehydration, quantification of H₂-TPD, reduction temperature effect, TEM, XANES spectra of Ni and Mo references, detailed EXAFS fitting result, CO chemisorption, NH₃-TPD and its relationship with dehydration reaction, O₂ chemisorption and its relationship with deoxygenation reaction, XRD of the used catalyst, stability test, XRD patterns and HDO performance of Mo/SiO₂ with different Mo loading and MoNi/SiO₂ catalysts with the same Mo loading and varying Ni loading, HRTEM of NiMo21 and EDS mapping of NiMo11 (PDF)

AUTHOR INFORMATION

Corresponding Authors

*E-mail: xinlizhu@tju.edu.cn. *E-mail: resasco@ou.edu.

ORCID ®

Jeffrey T. Miller: 0000-0002-6269-0620 Xinli Zhu: 0000-0002-8681-9994

Daniel E. Resasco: 0000-0001-5342-0621

Notes

The authors declare no competing financial interest.

ACKNOWLEDGMENTS

This research was funded by the National Natural Science Foundation of China (21676194), the Ministry of Education of China for Program of New Century Excellent talents in University (NECT-12-0407), and the U.S Department of Energy, Office of Science, Basic Energy Sciences under Award Number DE-SC0018284. F.Y was thankful for the support of the China Scholarship Council for the exchanged program to study at the University of Oklahoma. N.L. and J.T.M. were supported in part by the National Science Foundation under Cooperative Agreement No. EEC 1647722 and National

Science Foundation, Chemical, Engineering, Biological, and Transport Systems (CBET) division, award 1804712. MRCAT operations and beamline are supported by the Department of Energy and the MRCAT member institutions. This research used resources of 537 the Advanced Photon Source, a U.S. Department of Energy (DOE) Office of Science User Facility operated 538 for the DOE Office of Science by Argonne National Laboratory under Contract No. DE-AC02-06CH11357.

REFERENCES

- (1) Ragauskas, A. J.; Beckham, G. T.; Biddy, M. J.; Chandra, R.; Chen, F.; Davis, M. F.; Davison, B. H.; Dixon, R. A.; Gilna, P.; Keller, M.; Langan, P.; Naskar, A. K.; Saddler, J. N.; Tschaplinski, T. J.; Tuskan, G. A.; Wyman, C. E. Lignin valorization: improving lignin processing in the biorefinery. *Science* **2014**, *344* (6185), 1246843.
- (2) Huber, G. W.; Iborra, S.; Corma, A. Synthesis of Transportation Fuels from Biomass: Chemistry, Catalysts, and Engineering. *Chem. Rev.* 2006, 106, 4044–4098.
- (3) Zakzeski, J.; Bruijnincx, P. C. A.; Jongerius, A. L.; Weckhuysen, B. M. The Catalytic Valorization of Lignin for the Production of Renewable Chemicals. *Chem. Rev.* **2010**, *110*, 3552–3599.
- (4) Zacher, A. H.; Olarte, M. V.; Santosa, D. M.; Elliott, D. C.; Jones, S. B. A review and perspective of recent bio-oil hydrotreating research. *Green Chem.* **2014**, *16*, 491–515.
- (5) Furimsky, E. Catalytic hydrodeoxygenation. *Appl. Catal., A* **2000**, 199, 147–190.
- (6) Choudhary, T. V.; Phillips, C. B. Renewable fuels via catalytic hydrodeoxygenation. *Appl. Catal., A* **2011**, 397, 1–12.
- (7) Hicks, J. C. Advances in C-O Bond Transformations in Lignin-Derived Compounds for Biofuels Production. *J. Phys. Chem. Lett.* **2011**, 2, 2280–2287.
- (8) Saidi, M.; Samimi, F.; Karimipourfard, D.; Nimmanwudipong, T.; Gates, B. C.; Rahimpour, M. R. Upgrading of lignin-derived bio-oils by catalytic hydrodeoxygenation. *Energy Environ. Sci.* **2014**, *7*, 103–129.
- (9) Venkatakrishnan, V. K.; Delgass, W. N.; Ribeiro, F. H.; Agrawal, R. Oxygen removal from intact biomass to produce liquid fuel range hydrocarbons via fast-hydropyrolysis and vapor-phase catalytic hydrodeoxygenation. *Green Chem.* **2015**, *17*, 178–183.
- (10) Yoon, Y.; Rousseau, R.; Weber, R. S.; Mei, D.; Lercher, J. A. First-Principles Study of Phenol Hydrogenation on Pt and Ni Catalysts in Aqueous Phase. *J. Am. Chem. Soc.* **2014**, *136*, 10287–98.
- (11) Mortensen, P. M.; Grunwaldt, J. D.; Jensen, P. A.; Jensen, A. D. Screening of Catalysts for Hydrodeoxygenation of Phenol as a Model Compound for Bio-oil. *ACS Catal.* **2013**, *3*, 1774–1785.
- (12) Dickinson, J. G.; Savage, P. E. Development of NiCu Catalysts for Aqueous-Phase Hydrodeoxygenation. ACS Catal. **2014**, *4*, 2605–2615
- (13) Olcese, R. N.; Bettahar, M.; Petitjean, D.; Malaman, B.; Giovanella, F.; Dufour, A. Gas-phase hydrodeoxygenation of guaiacol over Fe/SiO₂ catalyst. *Appl. Catal., B* **2012**, *115–116*, 63–73.
- (14) Prasomsri, T.; Shetty, M.; Murugappan, K.; Román-Leshkov, Y. Insights into the catalytic activity and surface modification of MoO₃ during the hydrodeoxygenation of lignin-derived model compounds into aromatic hydrocarbons under low hydrogen pressures. *Energy Environ. Sci.* **2014**, *7*, 2660–2669.
- (15) Hong, Y.; Zhang, H.; Sun, J.; Ayman, K. M.; Hensley, A. J. R.; Gu, M.; Engelhard, M. H.; McEwen, J.-S.; Wang, Y. Synergistic Catalysis between Pd and Fe in Gas Phase Hydrodeoxygenation of m-Cresol. *ACS Catal.* **2014**, *4*, 3335–3345.
- (16) Romero, Y.; Richard, F.; Brunet, S. Hydrodeoxygenation of 2-ethylphenol as a model compound of bio-crude over sulfided Mobased catalysts: Promoting effect and reaction mechanism. *Appl. Catal., B* **2010**, *98*, 213–223.
- (17) Liu, G.; Robertson, A. W.; Li, M. M.; Kuo, W. C. H.; Darby, M. T.; Muhieddine, M. H.; Lin, Y. C.; Suenaga, K.; Stamatakis, M.; Warner, J. H.; Tsang, S. C. E. MoS₂ monolayer catalyst doped with

isolated Co atoms for the hydrodeoxygenation reaction. *Nat. Chem.* 2017, 9, 810–816.

- (18) Zhu, X.; Lobban, L. L.; Mallinson, R. G.; Resasco, D. E. Bifunctional transalkylation and hydrodeoxygenation of anisole over a Pt/HBeta catalyst. *J. Catal.* **2011**, 281, 21–29.
- (19) Nelson, R. C.; Baek, B.; Ruiz, P.; Goundie, B.; Brooks, A.; Wheeler, M. C.; Frederick, B. G.; Grabow, L. C.; Austin, R. N. Experimental and Theoretical Insights into the Hydrogen-Efficient Direct Hydrodeoxygenation Mechanism of Phenol over Ru/TiO₂. *ACS Catal.* **2015**, *5*, 6509–6523.
- (20) de Souza, P. M.; Rabelo-Neto, R. C.; Borges, L. E. P.; Jacobs, G.; Davis, B. H.; Sooknoi, T.; Resasco, D. E.; Noronha, F. B. Role of Keto Intermediates in the Hydrodeoxygenation of Phenol over Pd on Oxophilic Supports. *ACS Catal.* **2015**, *5*, 1318–1329.
- (21) Robinson, A.; Ferguson, G. A.; Gallagher, J. R.; Cheah, S.; Beckham, G. T.; Schaidle, J. A.; Hensley, J. E.; Medlin, J. W. Enhanced Hydrodeoxygenation ofm-Cresol over Bimetallic Pt-Mo Catalysts through an Oxophilic Metal-Induced Tautomerization Pathway. *ACS Catal.* **2016**, *6*, 4356–4368.
- (22) He, T.; Liu, X.; Ge, Y.; Han, D.; Li, J.; Wang, Z.; Wu, J. Gas phase hydrodeoxygenation of anisole and guaiacol to aromatics with a high selectivity over Ni-Mo/SiO₂. *Catal. Commun.* **2017**, *102*, 127–130.
- (23) Shetty, M.; Murugappan, K.; Prasomsri, T.; Green, W. H.; Román-Leshkov, Y. Reactivity and stability investigation of supported molybdenum oxide catalysts for the hydrodeoxygenation (HDO) of m-cresol. *J. Catal.* **2015**, *331*, 86–97.
- (24) Chen, C.; Chen, G.; Yang, F.; Wang, H.; Han, J.; Ge, Q.; Zhu, X. Vapor phase hydrodeoxygenation and hydrogenation of m-cresol on silica supported Ni, Pd and Pt catalysts. *Chem. Eng. Sci.* **2015**, *135*, 145–154.
- (25) Yang, F.; Liu, D.; Zhao, Y.; Wang, H.; Han, J.; Ge, Q.; Zhu, X. Size Dependence of Vapor Phase Hydrodeoxygenation of m-Cresol on Ni/SiO₂ Catalysts. *ACS Catal.* **2018**, *8*, 1672–1682.
- (26) Nie, L.; de Souza, P. M.; Noronha, F. B.; An, W.; Sooknoi, T.; Resasco, D. E. Selective conversion of m-cresol to toluene over bimetallic Ni-Fe catalysts. *J. Mol. Catal. A: Chem.* **2014**, 388–389, 47–55.
- (27) Tran, N. T. T.; Uemura, Y.; Chowdhury, S.; Ramli, A. Vaporphase hydrodeoxygenation of guaiacol on Al-MCM-41 supported Ni and Co catalysts. *Appl. Catal., A* **2016**, *512*, 93–100.
- (28) Yang, F.; Liu, D.; Wang, H.; Liu, X.; Han, J.; Ge, Q.; Zhu, X. Geometric and electronic effects of bimetallic Ni-Re catalysts for selective deoxygenation of m-cresol to toluene. *J. Catal.* **2017**, *349*, 84–97
- (29) Wang, M.; Zhang, X.; Li, H.; Lu, J.; Liu, M.; Wang, F. Carbon Modification of Nickel Catalyst for Depolymerization of Oxidized Lignin to Aromatics. ACS Catal. 2018, 8, 1614–1620.
- (30) Sachtler, W. M. H. Ensemble and Ligand Effects in Metal Catalysis. In *Handbook of Heterogeneous Catalysis*; Ertl, G., Knozinger, H., Weitkamp, J., Eds.; VCH: Weinheim, 1997; Vol. 3, pp 1585–1593.
- (31) Raikwar, D.; Munagala, M.; Majumdar, S.; Shee, D. Hydro-deoxygenation of guaiacol over Mo, W and Ta modified supported nickel catalysts. *Catal. Today* **2019**, 325, 117–130.
- (32) Phan, B. M. Q.; Ha, Q. L. M.; Le, N. P.; Ngo, P. T.; Nguyen, T. H.; Dang, T. T.; Nguyen, L. H.; Nguyen, D. A.; Luu, L. C. Influences of Various Supports, γ-Al₂O₃, CeO₂, and SBA-15 on HDO Performance of NiMo Catalyst. *Catal. Lett.* **2015**, *145*, 662–667.
- (33) Li, K.; Wang, R.; Chen, J. Hydrodeoxygenation of Anisole over Silica-Supported Ni₂P, MoP, and NiMoP Catalysts. *Energy Fuels* **2011**, 25, 854–863.
- (34) Smirnov, A. A.; Khromova, S. A.; Ermakov, D. Y.; Bulavchenko, O. A.; Saraev, A. A.; Aleksandrov, P. V.; Kaichev, V. V.; Yakovlev, V. A. The composition of Ni-Mo phases obtained by NiMoO_x-SiO₂ reduction and their catalytic properties in anisole hydrogenation. *Appl. Catal., A* **2016**, *514*, 224–234.
- (35) Hsu, P. J.; Jiang, J. W.; Lin, Y. C. Does a Strong Oxophilic Promoter Enhance Direct Deoxygenation? A Study of NiFe, NiMo,

- and NiW Catalysts in p-Cresol Conversion. ACS Sustainable Chem. Eng. 2018, 6, 660–667.
- (36) Wang, H.; Feng, M.; Yang, B. Catalytic hydrodeoxygenation of anisole: an insight into the role of metals in transalkylation reactions in bio-oil upgrading. *Green Chem.* **2017**, *19*, 1668–1673.
- (37) Selvaraj, M.; Shanthi, K.; Maheswari, R.; Ramanathan, A. Hydrodeoxygenation of Guaiacol over MoO₃-NiO/Mesoporous Silicates: Effect of Incorporated Heteroatom. *Energy Fuels* **2014**, 28, 2598–2607.
- (38) Yang, F.; Wang, H.; Han, J.; Ge, Q.; Zhu, X., Influence of Re addition to Ni/SiO₂ catalyst on the reaction network and deactivation during hydrodeoxygenation of m-cresol. *Catal. Today* **2018**, DOI: 10.1016/j.cattod.2018.04.073.
- (39) Boudart, M.; Mcconica, C. M. Catalytic hydrogenation of cyclohexene-gas phase reaction on supported Nickel. *J. Catal.* **1989**, 117, 33–41.
- (40) Aminzadeh, A.; Sarikhani-Fard, H. Raman spectroscopic study of Ni/Al₂O₃ catalyst. *Spectrochim. Acta, Part A* **1999**, *55*, 1421–1425.
- (41) Mestl, G.; Ruiz, P.; Delmon, B.; Knozinger, H. Oxygen-Exchange Properties of MoO₃ an in-Situ Raman-Spectroscopy Study. *J. Phys. Chem.* **1994**, *98*, 11269–11275.
- (42) Wachs, I. E. Raman and IR studies of surface metal oxide species on oxide. *Catal. Today* **1996**, 27, 437–455.
- (43) Dufresne, P.; Payen, E.; Grimblot, J.; Bonnelle, J. P. Study of nickel-molybdenum-gamma.-aluminum oxide catalysts by x-ray photoelectron and Raman spectroscopy. Comparison with cobalt-molybdenum-gamma.-aluminum oxide catalysts. *J. Phys. Chem.* **1981**, 85, 2344–2351.
- (44) Mile, B.; Stirling, D.; Zammitt, M. A.; Lovell, A.; Webb, M. The location of nickel oxide and nickel in silica-supported catalysts: Two forms of "NiO" and the assignment of temperature-programmed reduction profiles. *J. Catal.* **1988**, *114*, 217–229.
- (45) Calderón-Magdaleno, M. Á.; Mendoza-Nieto, J. A.; Klimova, T. E. Effect of the amount of citric acid used in the preparation of NiMo/SBA-15 catalysts on their performance in HDS of dibenzothiophenetype compounds. *Catal. Today* **2014**, 220–222, 78–88.
- (46) Halawy, S. A.; Mohamed, M. A.; Bond, G. C. Characterization of Unsupported Molybdenum Oxide Cobalt Oxide Catalysts. *J. Chem. Technol. Biotechnol.* **1993**, *58*, 237–245.
- (47) Miller, J. T.; Kropf, A. J.; Zha, Y.; Regalbuto, J. R.; Delannoy, L.; Louis, C.; Bus, E.; van Bokhoven, J. A. The effect of gold particle size on AuAu bond length and reactivity toward oxygen in supported catalysts. *J. Catal.* **2006**, 240, 222–234.
- (48) Haller, G. L.; Resasco, D. E. Metal-Support Interaction: Group VIII Metals and Reducible Oxides. *Adv. Catal.* **1989**, *36*, 173–235.
- (49) Tauster, S. J.; Fung, S. C.; Garten, R. L. Strong Metal-Support Interactions. Group 8 Noble Metals Supported on TiO₂. *J. Am. Chem. Soc.* **1978**, *100*, 170–175.
- (50) Resasco, D. E.; Haller, G. L. A Model of Metal-Oxide Support interaction for Rh on TiO₂. *J. Catal.* **1983**, 82, 279–288.
- (51) Raupp, G. B.; Dumesic, J. A. Effects of Titania on the Coadsorption of H₂ and CO on Nickel surfaces: Consequences for Understanding Methanation over Titania Supported Ni Catalysts. *J. Catal.* **1985**, *96*, 597–612.
- (52) Raupp, G. B.; Dumesic, J. A. Effect of Titania Surface Species on the Chemisorption of CO and $\rm H_2$ on Polycrystalline Nickel. *J. Phys. Chem.* **1984**, 88, 660–663.
- (53) Zhang, X.; Yan, P.; Zhao, B.; Liu, K.; Kung, M. C.; Kung, H. H.; Chen, S.; Zhang, Z. C. Selective Hydrodeoxygenation of Guaiacol to Phenolics by Ni/Anatase TiO₂ Catalyst Formed by Cross-Surface Migration of Ni and TiO₂. ACS Catal. **2019**, *9*, 3551–3563.
- (54) Tsurov, M. A.; Afanasiev, P. V.; Lunin, V. V. Composition and Catalytic Properties of Products from the Reduction of NiMoO₄. *Appl. Catal., A* **1993**, *105*, 205–221.
- (55) Murugappan, K.; Anderson, E. M.; Teschner, D.; Jones, T. E.; Skorupska, K.; Román-Leshkov, Y. Operando NAP-XPS unveils differences in MoO_3 and Mo_2C during hydrodeoxygenation. *Nat. Catal.* **2018**, *1*, 960–967.